

# Two-neutron overlap functions for $^6\text{He}$ from a microscopic structure model

I. Brida<sup>a b \*</sup>, F.M. Nunes<sup>a</sup>

<sup>a</sup>NSCL and Department of Physics and Astronomy, Michigan State University, East Lansing, MI 48824, USA

<sup>b</sup>Physics Division, Argonne National Laboratory, Argonne, IL 60439, USA

A fully antisymmetrized microscopic model is developed for light two-neutron halo nuclei using a hyper-spherical basis to describe halo regions. The many-body wavefunction is optimized variationally. The model is applied to  $^6\text{He}$  bound by semi realistic Minnesota nucleon-nucleon forces. The two-neutron separation energy and the radius of the halo are reproduced in agreement with experiment. Antisymmetrization effects between  $^4\text{He}$  and halo neutrons are found to be crucial for binding of  $^6\text{He}$ . We also properly extract two-neutron overlap functions and find that there is a significant increase of 30%-70% in their normalization due to microscopic effects as compared to the results of three-body models.

## 1. Introduction

In some light nuclei, the proximity to particle emission thresholds allows loosely bound nucleons to tunnel out into the classically forbidden region and form what is typically referred to as a *halo*. One neutron halos, such as  $^{11}\text{Be}$  and  $^{19}\text{C}$ , and two-neutron halos, such as  $^6\text{He}$  and  $^{11}\text{Li}$ , are the most common, although there are nuclear states with the halo formed by protons or more than two neutrons. All these systems have very small separation energies and unusually large matter radii, when compared to neighboring nuclei, and many of their properties are determined by the long-range part of the many-body wavefunction. Halo systems are not specific to nuclear physics; a review covering a number of fields can be found in [ 1]. In this work, we focus on two-neutron halo nuclei in which long-range Coulomb effects are not present.

Traditionally, the theory of halo nuclei has been dominated by simple few-body models. These models place their faith on the fact that the valence particles forming the halo are partially decoupled from the rest of the system, the core. In this frame of mind, one typically assumes that the core degrees of freedom are completely frozen, while meticulously treating the relative motion between the valence nucleons and the core. Then, the many-body problem containing a two-neutron halo reduces to a core+n+n three-body one. For an overview of three-body techniques applied to halo nuclei, see for example [ 2].

---

\*Corresponding author: brida@anl.gov

The crucial assumption of few-body models, a macroscopic inert core, is a mixed blessing: on one hand, it allows one to focus on the long-range core-valence correlations, on the other hand, it is undoubtedly a crude simplification of the many-body problem. Stemming from the inert core employed, the main drawbacks of three-body models are: i) unknown properties of the core, i.e. the internal details of the core are left out completely and, only when needed, they are provided in an ad hoc manner, ii) the improper treatment of antisymmetrization [ 3], iii) the use of effective core-nucleon interactions constructed case by case in an ambiguous manner, and iv) the fact that even when the two-body interactions are fitted to (some) properties of all two-body subsystems, the resulting three-body separation energy is (much) smaller than the experimental value [ 2, 4]. This pathological lack of binding is often cured with an empirical three-body force or the two-body forces are refitted to deliver the right three-body binding. Furthermore, there are indications that for reaction calculations three-body wavefunctions may require additional renormalization to account for microscopic effects missing in the inert-core approximation [ 5]. Some improvement over the inert-core picture is provided by few-body models incorporating collective excitations into the core [ 6, 7, 8]; they, however, still suffer from the above-mentioned drawbacks of few-body models, and in addition are limited to applications where the core is a good rotor or vibrator. Given all these drawbacks, the predictive power of three-body models of two-neutron halo nuclei is rather limited.

The above-mentioned drawbacks of few-body models are eliminated in microscopic (cluster) models of light nuclei. Over the last decade, there have been tremendous advances in brute force ab-initio methods and due to increasing computational power, these models have improved their accuracy and predictability. Amongst these, the Green's function Monte Carlo (GFMC) [ 9, 10], the no-core shell model [ 11, 12, 13], and molecular dynamics models [ 14, 15, 16] have been successfully applied to light s- and p-shell nuclei. Somewhere between few-body and ab-initio models are microscopic cluster models in which some degrees of freedom are frozen to reduce the complexity of the many-body problem. Of particular relevance to this work is the stochastic variational method (SVM) [ 17, 18] which inspired several aspects of the model here presented. Applications of SVM and some other cluster models to two-neutron halo nuclei can be found for example in [ 19, 20, 21, 22, 23].

Despite the success of existing microscopic (cluster) models applied to non-halo nuclei and their ability to reproduce basic properties of some halo species, such as (three-body) binding energies and radii, questions may arise about their ability to capture the long-range halo correlations. These correlations are important because the halo nucleons spend a considerable amount of time in regions distant from the core and, generally, it is this part of configuration space that contributes the most to reaction observables. As is known from three-body models, the wavefunction describing a two-neutron halo nucleus ought to fall off exponentially. Existing microscopic structure models do not pay close attention (if any) to asymptotic regions, instead they use the binding energy to assess the convergence towards an eigenstate. The convergence of the energy, however, does not necessarily guarantee the convergence of the wavefunction in long-range regions. Moreover, most microscopic models exploit computationally tractable bases, most commonly Gaussians of one sort or the other. In principle, it should be possible to capture the slower exponential decay by using a large Gaussian basis, but as argued in [ 1], quality precedes quantity

when it comes to halo nuclei; that is the shape of the basis functions matters more than the size of the basis.

In addition, existing microscopic structure models fail to provide input to reaction calculations of two-neutron halo nuclei. To feed reaction calculations, by themselves formulated in a few-body picture, one would have to extract information about halo particles from a full microscopic wavefunction which is a non-trivial task. Even though recently we have witnessed some progress in this direction for two-body non-halo projectiles [ 24, 25], most microscopic structure theories are still far from providing such few-body-like information about three-body-like halo nuclei. It is for this reason that in reaction calculations the structure of halo nuclei is taken from few-body models despite all their drawbacks.

It is obvious that both few-body and microscopic structure models have their appealing aspects as well as drawbacks. It is the aim of this work to combine the best of the two worlds: to develop a fully microscopic model for light two-neutron halo nuclei bound by nucleon-nucleon interactions that would describe simultaneously short- and especially long-distance regions. The novelty of our model is the integration of few-body and ab-initio methods. We use a basis that describes short-range correlations and at the same time preserves the correct three-body asymptotics. This is achieved at a high computational cost since matrix elements cannot be evaluated analytically. Our ultimate goal is to provide microscopic structure information to be used in reaction calculations involving two-neutron halo nuclei.

In this paper our model is applied to the simplest two-neutron halo nucleus,  ${}^6\text{He}$ . Preliminary results for this case have been published in [ 26]. Since neither  ${}^5\text{He}$  thought of as  ${}^4\text{He} + \text{n}$  nor the  $\text{n} + \text{n}$  subsystem are bound,  ${}^6\text{He}$  is a Borromean system [ 2]. To provide input for reaction calculations involving this nucleus, two-neutron overlap functions are properly computed from our microscopic model and, to our best knowledge, they are for the first time expressed in hyper-spherical coordinates. By doing so, these functions are directly applicable to some reaction calculations and they can be compared directly to three-body wavefunctions.

This paper is organized as follows. In Section 2, the theoretical formulation of our model is developed. Section 3 outlines some technical details and numerical procedures employed. Results for  ${}^6\text{He}$  are discussed in Section 4. A summary can be found in Section 5 along with an outlook of possible future developments.

## 2. Theory

The model here presented has as its primary goal the applicability to reactions involving light two-neutron halo nuclei and thus needs to capture few-body long-distance features of these systems. A two-neutron halo nucleus will be described by an antisymmetrized product of a microscopic core and a valence part consisting of two neutrons, or schematically  $\Psi = \mathcal{A}^{\text{core-val}}(\text{core} \times \text{valence})$ . The terms “core” and “valence” refer to distinct pieces of the wavefunction prior to the action of the core-valence antisymmetrizer  $\mathcal{A}^{\text{core-val}}$  upon which nucleons from the two parts of the wavefunction become indistinguishable. At large distances, our wavefunction decouples into the three-body-like form  $\Psi \rightarrow \text{core} \times \text{n} \times \text{n}$  of a desired shape most naturally expressed in Jacobi coordinates. It was therefore our choice from the early start to express the entire wavefunction in Jacobi coordinates. As

an additional benefit of using these coordinates, translational invariance is guaranteed. All details of the model can be found in [ 27].

More precisely, the microscopic core with a fixed total angular momentum and parity  $J_{core}^\pi$ , and isospin  $T_{core}$  with projection  $M_{T_{core}}$  is described by an antisymmetrized wavefunction  $\Phi_{J_{core}^\pi T_{core} M_{T_{core}}}$  corresponding to the core's ground state. If desired, excited states of the core can be included in the future. The valence terms are drawn from a suitable hyper-spherical basis. Each valence basis function  $\psi$  carries total angular momentum  $J_{val}^\pi$ , and isospin  $T_{val}$  with projection  $M_{T_{val}}$ , which coupled to the core's quantum numbers give  $J^\pi$ ,  $T$ , and  $M_T$  for the full system. For neutron-rich two-neutron halo nuclei, such as  $^6\text{He}$  and  $^{11}\text{Li}$ ,  $T_{val} = 1$  and  $M_{T_{val}} = -1$ , and the core-valence isospin coupling is trivial. It is understood that parities  $\pi$  carry the same subscripts as their corresponding  $J$  and that  $\pi = \pi_{core}\pi_{val}$ . Then, the total wavefunction is written as:

$$\Psi_{J^\pi M_J T M_T} = \sum c_{J_{core}^\pi \Gamma_{val} J_{val}^\pi} \mathcal{A}^{core-val} [\Phi_{J_{core}^\pi T_{core} M_{T_{core}}} \otimes \mathcal{A}^{val} \psi_{\Gamma_{val} J_{val}^\pi 1-1}]_{J^\pi M_J T M_T}. \quad (1)$$

By acting on valence particles only, the operator  $\mathcal{A}^{val} = \sum_1^2 (-1)^p P$  antisymmetrizes the valence part, whereas the core-valence antisymmetrizer  $\mathcal{A}^{core-val} = \sum_1^{A(A-1)/2} (-1)^p P$  permutes valence particles with those inside the core. In these operators,  $P$  are permutation operators,  $p$  are permutation parities, and  $A = A_{core} + 2$  is the mass number of the halo nucleus. The meaning of  $\Gamma_{val}$  is explained in Section 2.2.

The wavefunction in Eq. (1) is constructed in two steps. First, the wavefunction of the core as a free nucleus is built within SVM, as briefly described in Section 2.1. Unlike many microscopic cluster models employing a simple 0s-harmonic oscillator approximation to  $^4\text{He}$ , we use the best possible wavefunction for the core obtainable within SVM. By doing so, we hope to attenuate the problem of underbinding relative to the three-body threshold [ 19, 28]. Once the core wavefunction is optimized, its parameters remain unchanged in the subsequent minimization procedure. This implies that, as in other microscopic cluster models, distortion of the core due to valence neutrons is not accounted for explicitly, although some distortion is delivered through the core-valence antisymmetrization. In the second step, the valence part is constructed by drawing terms  $\psi_{\Gamma_{val} J_{val}^\pi 1-1}$  from a hyper-spherical basis described in Section 2.2. Valence basis functions contain discrete as well as non-linear continuous parameters that are optimized variationally, along with the linear coefficients  $c$  in Eq. (1), by minimizing the expectation value of the Hamiltonian  $H$ :

$$E = \frac{\langle \Psi | H | \Psi \rangle}{\langle \Psi | \Psi \rangle} \quad (2)$$

as outlined in Section 3. To feed reaction calculations involving nuclei of interest, two-neutron overlap functions are extracted from the resulting optimized wavefunctions, as presented in Section 2.4.

## 2.1. The core in SVM

Our choice of the microscopic model for the core has been motivated by the following factors. The model should provide accurate structure for the core; it needs to be extendable to cores heavier than  $^4\text{He}$ ; and it must handle central and non-central nucleon-nucleon

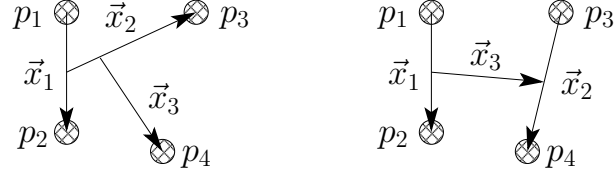


Figure 1. Sets of relative Jacobi coordinates  $\vec{x}$  for a four-particle ( $p_1, \dots, p_4$ ) system: K-like (left) and H-like (right). Each Jacobi coordinate connects centers of masses of subgroups of particles.

forces. Unlike for the valence part, there is no need to impose special asymptotic requirements on the core. Finally, as mentioned earlier in this section, the wavefunction of the core should be expressed in Jacobi coordinates. It is for these reasons that the SVM model seemed to be the most appropriate. In this section, basic ingredients of SVM applied to  ${}^4\text{He}$  are outlined; more details on the method can be found in [ 17, 18, 27].

In SVM, the core wavefunction is written as a linear combination of basis functions  $\phi$ :

$$\Phi_{J_{\text{core}}^{\pi} T_{\text{core}} M_{T_{\text{core}}}} = \mathcal{A}^{\text{core}} \sum c_{\Gamma_{\text{core}} J_{\text{core}}^{\pi} T_{\text{core}} M_{T_{\text{core}}}} \phi_{\Gamma_{\text{core}} J_{\text{core}}^{\pi} T_{\text{core}} M_{T_{\text{core}}}} \quad (3)$$

with the projection of  $J_{\text{core}}$  suppressed. The operator  $\mathcal{A}^{\text{core}}$  antisymmetrizes particles inside the core. Basis states  $\phi$  take the form of correlated Gaussians expressed in Jacobi coordinates. For a four-particle system, there exist two different—K- and H-like—sets of Jacobi coordinates  $\vec{x} \equiv \{\vec{x}_1, \vec{x}_2, \vec{x}_3\}$  as shown in Figure 1. To accelerate the optimization of the core’s wavefunction, both Jacobi sets enter Eq. (3) as they invoke different inter-particle correlations. For  ${}^4\text{He}$ , a basis term in either Jacobi basis is given by:

$$\phi_{\Gamma_{\text{core}} J_{\text{core}}^{\pi} T_{\text{core}} M_{T_{\text{core}}}} (\vec{x}, \mathbf{A}) = \exp \left( -\frac{1}{2} \vec{x} \mathbf{A} \vec{x} \right) [\theta_{l_1 l_2 l_3 L_{12} L} (\vec{x}) \otimes \chi_{S_{12} S_{123} S}]_{J_{\text{core}}^{\pi}} \tau_{T_{12} T_{123} T_{\text{core}} M_{T_{\text{core}}}}. \quad (4)$$

The function  $\theta_{l_1 l_2 l_3 L_{12} L} (\vec{x})$  is taken as a vector-coupled product of solid harmonics [ 29]:

$$\theta_{l_1 l_2 l_3 L_{12} L} (\vec{x}) = [[\mathcal{Y}_{l_1} (\vec{x}_1) \otimes \mathcal{Y}_{l_2} (\vec{x}_2)]_{L_{12}} \otimes \mathcal{Y}_{l_3} (\vec{x}_3)]_L. \quad (5)$$

The spin  $\chi_{S_{12} S_{123} S}$  and isospin  $\tau_{T_{12} T_{123} T_{\text{core}} M_{T_{\text{core}}}}$  parts consist of successively coupled single-particle spins and isospins:

$$\chi_{S_{12} S_{123} S} = \left[ [[\chi_{p_1} \otimes \chi_{p_2}]_{S_{12}} \otimes \chi_{p_3}]_{S_{123}} \otimes \chi_{p_4} \right]_S, \quad (6)$$

$$\tau_{T_{12} T_{123} T_{\text{core}} M_{T_{\text{core}}}} = \left[ [[\tau_{p_1} \otimes \tau_{p_2}]_{T_{12}} \otimes \tau_{p_3}]_{T_{123}} \otimes \tau_{p_4} \right]_{T_{\text{core}} M_{T_{\text{core}}}}. \quad (7)$$

For  ${}^4\text{He}$ , the Gaussian part in Eq. (4) contains a  $(3 \times 3)$ -dimensional positive-definite, symmetric matrix  $\mathbf{A}$ , specific to each basis term. The quadratic form  $\vec{x} \mathbf{A} \vec{x}$  involves scalar

products of Jacobi vectors:

$$x \mathbf{A} x \equiv \sum_{i,j=1}^3 \mathbf{A}_{ij} \vec{x}_i \cdot \vec{x}_j. \quad (8)$$

Due to the symmetry requirement, the matrix  $\mathbf{A}$  has only 6 independent elements and they are considered non-linear continuous variational parameters. Note that, although the Gaussian in Eq. (4) as a whole is a spherically symmetric object, it still carries angular information due to cross terms  $\vec{x}_i \cdot \vec{x}_j$  when the matrix  $\mathbf{A}$  is non-diagonal as considered here. In such a case, numbers  $l_1, l_2, l_3$  in Eq. (5) loose their meaning of orbital momentum quantum numbers and can be treated as discrete variational parameters, instead.

The composite index  $\Gamma_{core}$  comprises other (quantum) numbers, elements of the matrix  $\mathbf{A}$ , and the Jacobi channel identifier K or H, i.e.  $\Gamma_{core} = \{l_1, l_2, l_3, L_{12}, L, S_{12}, S_{123}, S, T_{12}, T_{123}, K/H, \mathbf{A}\}$ . The sum in Eq. (3) was left without a summation index because in SVM the wavefunction  $\Phi$  is constructed term by term by minimizing the expectation value of energy with all components of  $\Gamma_{core}$  optimized stochastically. Linear expansion coefficients  $c$  in Eq. (3) are determined via energy matrix diagonalization.

## 2.2. The valence part in the hyper-spherical formalism

To inspire the form of valence functions in Eq. (1), let us first consider a few-body approach in which a two-neutron halo nucleus is treated as a three-body core+n<sub>1</sub>+n<sub>2</sub> system. From among all three-body models, we adopt the formalism of [ 30] and [ 31, pg. 278]. For all necessary details, see [ 27].

For a three-body core+n<sub>1</sub>+n<sub>2</sub> system, one can define two different—Y- and T-like—sets of Jacobi coordinates  $\vec{x} \equiv \{\vec{x}_1, \vec{x}_2\}$  as shown in Figure 2. These coordinates are further transformed into hyper-spherical coordinates  $\{\rho, \theta, \hat{x}\}$  where  $\hat{x} \equiv \{\hat{x}_1, \hat{x}_2\}$  are spherical angles corresponding to vectors  $\vec{x}$ . The hyper-radius  $\rho$  is related to the overall size of the system, while the hyper-angle  $\theta$  contains information about relative magnitudes of  $\vec{x}_1$  and  $\vec{x}_2$ . In three-body models, the use of hyper-spherical coordinates is motivated by the facts that: i) the three-body Schrödinger equation reduces to a one-dimensional hyper-radial differential equation, and ii) more importantly for us, in the absence of long-range forces the three-body wavefunction of Borromean systems decays asymptotically for  $\rho \rightarrow \infty$  as:

$$\rho^{-5/2} \exp(-\kappa\rho), \quad \kappa^2 = 2m |E_{3body}| / \hbar^2, \quad (9)$$

where  $E_{3body}$  is the binding energy relative to the three-body core+n+n threshold, and  $m$  is the mass of a nucleon. In hyper-spherical coordinates, the volume element becomes:

$$dV = (\mu_1 \mu_2)^{-3/2} \rho^5 \sin^2 \theta \cos^2 \theta d\rho d\theta d\hat{x}_1 d\hat{x}_2, \quad (10)$$

where  $\mu_i$ ,  $i = 1, 2$  are dimensionless reduced mass factors corresponding to vectors  $\vec{x}_i$ .

Upon the hyper-spherical transformation, the spatial part of the three-body wavefunction can be separated into its hyper-radial, hyper-angular, and spherical parts, each of which can be conveniently expanded. The spherical part is written as a coupled product of spherical harmonics  $Y_{l_1 m_1}(\hat{x}_1)$  and  $Y_{l_2 m_2}(\hat{x}_2)$ . The hyper-angular part is expanded over eigenstates  $\varphi_K^{l_1 l_2}(\theta)$  of the grand-angular operator appearing in the hyper-radial



Figure 2. Sets of relative Jacobi coordinates for a three-body core+ $n_1+n_2$  system: Y-like (left) and T-like (right). Each Jacobi coordinate connects centers of masses of subgroups of objects. These coordinates are not to be confused with those for the core in Figure 1.

Schrödinger equation. These functions are explicitly defined in terms of Jacobi polynomials  $P_{n_{jac}}^{l_1+\frac{1}{2}, l_2+\frac{1}{2}}$  of the order  $n_{jac} = 0, 1, 2, \dots$  with hyper-momentum  $K = l_1 + l_2 + 2n_{jac}$ :

$$\varphi_K^{l_1 l_2}(\theta) = N_K^{l_1 l_2} (\mu_1 \mu_2)^{3/4} \sin^{l_1} \theta \cos^{l_2} \theta P_{n_{jac}}^{l_1+\frac{1}{2}, l_2+\frac{1}{2}}(\cos 2\theta). \quad (11)$$

The normalization constant  $N_K^{l_1 l_2}$  is chosen to make these functions orthonormal with respect to a weight from the hyper-spherical volume element in Eq. (10):

$$\int_0^{\pi/2} \varphi_K^{l_1 l_2}(\theta) \varphi_{K'}^{l_1 l_2}(\theta) (\mu_1 \mu_2)^{-3/2} \sin^2 \theta \cos^2 \theta d\theta = \delta_{K, K'}. \quad (12)$$

Having in mind the importance of the asymptotic behavior of the wavefunction in Eq. (9), the three-body model in [ 30] employs a hyper-radial basis from [ 32] with the desired exponential trend built into it:

$$\mathcal{R}_{n_{lag}}(\rho, \rho_0) = \frac{1}{\rho_0^3} \sqrt{\frac{n_{lag}!}{(n_{lag} + 5)!}} L_{n_{lag}}^5 \left( \frac{\rho}{\rho_0} \right) \exp \left( -\frac{1}{2} \frac{\rho}{\rho_0} \right), \quad n_{lag} = 0, 1, 2, \dots. \quad (13)$$

Here,  $L_{n_{lag}}^5$  are associated Laguerre polynomials of the order  $n_{lag}$ . Note that this basis is just a suitable mathematical basis whose elements cannot be interpreted as hyper-radial eigenfunctions of the physical three-body system. Basis functions  $\mathcal{R}_{n_{lag}}$  are orthonormal with respect to the weight factor  $\rho^5$  from the volume element in Eq. (10):

$$\int_0^\infty \mathcal{R}_{n_{lag}}(\rho, \rho_0) \mathcal{R}_{n'_{lag}}(\rho, \rho_0) \rho^5 d\rho = \delta_{n_{lag}, n'_{lag}}. \quad (14)$$

The completeness of the hyper-radial basis for any  $\rho_0 > 0$  allows one to use any value of  $\rho_0$ , and yet reconstruct the asymptotically correct form of Eq. (9) determined by an a priori unknown three-body binding energy. The index  $n_{lag}$  is independent from quantum numbers attached to spherical and hyper-angular parts of the wavefunction.

Based on these three-body arguments, we have chosen for each valence term in Eq. (1) the following form:

$$\psi_{\Gamma_{val} J_{val}^\pi 1-1} = \mathcal{R}_{n_{lag}}(\rho, \rho_0) \mathcal{Y}_{\gamma_{val} J_{val}^\pi 1-1}(\theta, \hat{x}), \quad \Gamma_{val} = \{n_{lag}, \rho_0, \gamma_{val}\}, \quad (15)$$

where  $\mathcal{Y}$  is a generalized hyper-harmonic function in LS-coupling:

$$\mathcal{Y}_{\gamma_{val} J_{val}^{\pi} 1-1}(\theta, \hat{x}) = \varphi_K^{l_1 l_2}(\theta) \left[ [Y_{l_1}(\hat{x}_1) \otimes Y_{l_2}(\hat{x}_2)]_L \otimes [\chi_{n_1} \otimes \chi_{n_2}]_S \right]_{J_{val}^{\pi}} [\tau_{n_1} \otimes \tau_{n_2}]_{1-1}. \quad (16)$$

Here,  $\chi_{n_i}$  and  $\tau_{n_i}$  are spinors and isospinors of valence neutrons. The composite index  $\gamma_{val}$  comprises all other numbers as well as the Jacobi channel identifier Y or T, i.e.  $\gamma_{val} = \{K, l_1, l_2, L, S, Y/T\}$ . By construction, hyper-harmonics  $\mathcal{Y}$  corresponding to a given Jacobi basis are orthonormal in all components of  $\gamma_{val}$ . In the T Jacobi basis, the Pauli principle between valence neutrons is satisfied by requiring  $l_1 + S = \text{even}$ ; in the Y Jacobi basis, the exclusion principle is satisfied upon the action of  $\mathcal{A}^{val}$  in Eq. (1). Valence angular momenta  $l_1$ ,  $l_2$ ,  $L$ , and  $S$  are not to be confused with those for the core in Section 2.1.

### 2.3. The Hamiltonian

In this work, the nuclear Hamiltonian includes kinetic energies  $T_i$  of all nucleons and two-body nucleon-nucleon potentials  $V_{ij}$ :

$$H = \sum_{i=1}^A T_i + \sum_{1=i < j}^A V_{ij}. \quad (17)$$

No correction is needed for the kinetic energy of the total center of mass as the wavefunction in Eq. (1) is expressed in relative Jacobi coordinates.

In microscopic calculations, the choice of the effective nucleon-nucleon interaction is of crucial importance unless realistic forces are used. If a model is to have anything to do with the real physical problem, one must make sure that the inter-nucleon force is appropriate for all subsystems appearing in the model. In  ${}^6\text{He}$ , valence neutrons are mostly in spin-singlet configurations [ 2, 28]. The spin-singlet di-neutron state is unbound; however, many effective nucleon-nucleon interactions, such as the Volkov force [ 33], do not distinguish this state from a bound spin-triplet neutron-proton state, the deuteron.

In this work we use the semi-realistic Minnesota interaction [ 34]. This force reproduces the most important low-energy nucleon-nucleon scattering data and therefore it does not bind the di-neutron. The force renormalizes effects of the tensor force into its central component and binds the deuteron by the right amount assuming a proton and a neutron in a relative s-wave. It also gives realistic results for the bulk properties of nuclei in the lowest s-shell. Besides the central component, the potential contains spin, isospin, and spin-isospin exchange terms. The potential contains the mixture parameter  $u$  which can be tuned slightly to adjust the interaction strength. When supplemented by a spin-orbit force [ 35], the Minnesota interaction reproduces low-energy  $\alpha$ -nucleon scattering data. In [ 34], it is advised to employ a short-range spin-orbit force; on that merit we use the spin-orbit parameter set IV from Table 1 in [ 35].

In Section 4, we mostly show results obtained for the Minnesota plus the spin-orbit interaction (MN-SO). For comparative purposes, some calculations were performed in the absence of the spin-orbit force (MN). To reproduce the two-neutron separation energy 0.97 MeV of  ${}^6\text{He}$ , the mixture parameter  $u$  is changed from its default value 1.0 to 1.015 (MN-SO) and 1.15 (MN). By doing so, we expect to obtain a realistic description of the

halo even though the absolute binding of  $^4\text{He}$  and  $^6\text{He}$  is not reproduced. Essentially, the interaction mixture parameter is the only free parameter in our model. The Coulomb interaction is neglected as it should not affect the long-range behaviour of the neutron halo.

#### 2.4. Two-nucleon overlap functions

Once the full wavefunction in Eq. (1) is optimized as outlined in Section 3, one can use it to calculate various observables. Although most of the observables we calculate are standard, two-nucleon overlap functions deserve special attention. For general considerations regarding these functions, see [ 36, sect. 16.4.2] and [ 37].

The overlap integral between a two-neutron halo nucleus ( $\Psi$ ) described microscopically by Eq. (1) and its own core in the ground state ( $\Phi$ ) is defined as:

$$\mathcal{I}_{M_{val} 1-1} = \sqrt{\binom{A}{2}} \langle \Phi_{J_{core}^{\pi} M_{J_{core}} T_{core} M_{T_{core}}} | \Psi_{J^{\pi} M_J T M_T} \rangle. \quad (18)$$

The binomial factor accounts for the number of combinations to pick two out of  $A$  nucleons. The integration is done over all degrees of freedom in the core, and so the overlap integral  $\mathcal{I}$  depends only on the degrees of freedom of two valence<sup>2</sup> neutrons remaining outside the core. For neutron-rich two-neutron halo nuclei, the integral has a well defined isospin and its projection, 1 and -1, respectively, but it does not have a good angular momentum. The integral can, however, be expanded in a complete set of hyper-harmonics of angular momentum  $J_{val}^{\pi}$  introduced in Eq. (16):

$$\mathcal{I}_{M_{val} 1-1} = \sum_{\gamma_{val} J_{val}^{\pi}} C_{J_{core}^{\pi} M_{J_{core}} J_{val} M_{J_{val}}}^{JM_J} \mathcal{O}_{\gamma_{val} J_{val}^{\pi}}(\rho) \mathcal{Y}_{\gamma_{val} J_{val}^{\pi} 1-1}, \quad (19)$$

where  $C$  are Clebsch-Gordan coefficients. The expansion is carried out in the T Jacobi basis where the hyper-harmonics  $\mathcal{Y}$  satisfy the Pauli principle between valence neutrons by construction (see Section 2.2). The hyper-radial part in Eq. (19) is not expanded in the Laguerre basis from Eq. (13) because the basis functions  $\mathcal{R}_{n_{lag}}$  do not have physical significance. Instead, the overlap functions  $\mathcal{O}$  are computed directly from:

$$\mathcal{O}_{\gamma_{val} J_{val}^{\pi}}(\rho') = \sqrt{\binom{A}{2}} \left\langle \left[ \Phi_{J_{core}^{\pi} T_{core} M_{T_{core}}} \otimes \mathcal{Y}_{\gamma_{val} J_{val}^{\pi} 1-1} \right]_{J^{\pi} M_J T M_T} \left| \frac{\delta(\rho - \rho')}{\rho^5} \right| \Psi_{J^{\pi} M_J T M_T} \right\rangle \quad (20)$$

with the integration carried over degrees of freedom of all nucleons. A meaningful calculation of overlap functions  $\mathcal{O}$  requires both wavefunctions  $\Phi$  and  $\Psi$  to be normalized. Using overlap functions, a three-body-like core+n+n component of the wavefunction  $\Psi$  can be written as:

$$\Psi_{J^{\pi} M_J T M_T}^{overlap} = \sum_{\gamma_{val} J_{val}^{\pi}} \mathcal{O}_{\gamma_{val} J_{val}^{\pi}} \left[ \Phi_{J_{core}^{\pi} T_{core} M_{T_{core}}} \otimes \mathcal{Y}_{\gamma_{val} J_{val}^{\pi} 1-1} \right]_{J^{\pi} M_J T M_T} \quad (21)$$

---

<sup>2</sup>In the overlap integral, the two distinct neutrons outside the core are called “valence” They are not to be confused with neutrons in the valence part of the wavefunction in Eq. (1) where valence and core particles become indistinguishable upon the full antisymmetrization.

in a form analogous to that of the three-body wavefunction [ 30]. Note, however, that the core  $\Phi$  in Eq. (21) is fully microscopic, whereas the three-body wavefunction would contain an inert macroscopic core. Generally, the expansion in Eq. (21) would be a part of the fractional-parentage expansion of  $\Psi$ .

Overlap functions  $\mathcal{O}$  satisfy a three-body-like Schrödinger equation with a source term [ 37]. Therefore, at least in the asymptotic region, wavefunctions from three-body models and our microscopically founded overlap function  $\Psi^{overlap}$  should behave similarly. On this merit, we can compare our results with those from three-body models at the level of wavefunctions rather than integrated observables. An overlap term characterized by  $\gamma_{val}$  is referred to as an overlap or a three-body channel.

For practical considerations, it is convenient to introduce modified overlap functions:

$$u(\rho) = \rho^{5/2} \mathcal{O}(\rho) \quad (22)$$

with a regular behavior near the origin. Again, in the absence of long-range forces in Borromean-like nuclei, overlap functions decay as:

$$\mathcal{O}(\rho) \xrightarrow{\rho \rightarrow \infty} \rho^{-5/2} \exp(-\kappa\rho), \quad u(\rho) \xrightarrow{\rho \rightarrow \infty} \exp(-\kappa\rho) \quad (23)$$

just like three-body wavefunctions in Eq. (9). Formally, the decay constant  $\kappa$  in Eq. (23) is defined as in Eq. (9), the main difference is that for overlap functions the three-body binding energy needs to be computed microscopically. For the Borromean nucleus  ${}^6\text{He}$ :

$$E_{3body} = E({}^6\text{He}) - E({}^4\text{He}) \quad (24)$$

where  $E({}^6\text{He})$  and  $E({}^4\text{He})$  are binding energies corresponding to  $\Psi$  and  $\Phi$ , respectively.

Given the orthonormality of hyper-harmonics in Section 2.2, the norms—spectroscopic factors—of overlap channels are given by:

$$S_{\gamma_{val} J_{val}^\pi} = \int_0^\infty \mathcal{O}_{\gamma_{val} J_{val}^\pi}^2(\rho) \rho^5 d\rho = \int_0^\infty u_{\gamma_{val} J_{val}^\pi}^2(\rho) d\rho. \quad (25)$$

In three-body models, spectroscopic factors give the probability of finding the system in a given channel  $\gamma_{val}$ .

### 3. Numerical details

In Figure 3, we show the convergence of the binding energy of  ${}^4\text{He}$  with the number of Gaussians included in the SVM wavefunction described in Section 2.1. In converged MN and MN-SO (see Section 2.3) states containing 20 and 75 basis states,  ${}^4\text{He}$  is bound by -30.85 MeV and -30.93 MeV, respectively. In both cases, all channels with  $l \leq 2$  in Eq. (5) were present in the model space.

The expectation value of energy in Eq. (2) involves multidimensional integrals which must be evaluated efficiently to perform a meaningful variational calculation. For example in SVM employing the basis of correlated Gaussians, many matrix elements can be evaluated analytically in closed form, and consequently SVM can afford a random trial-and-error variational search. In our model, however, the core is combined with a

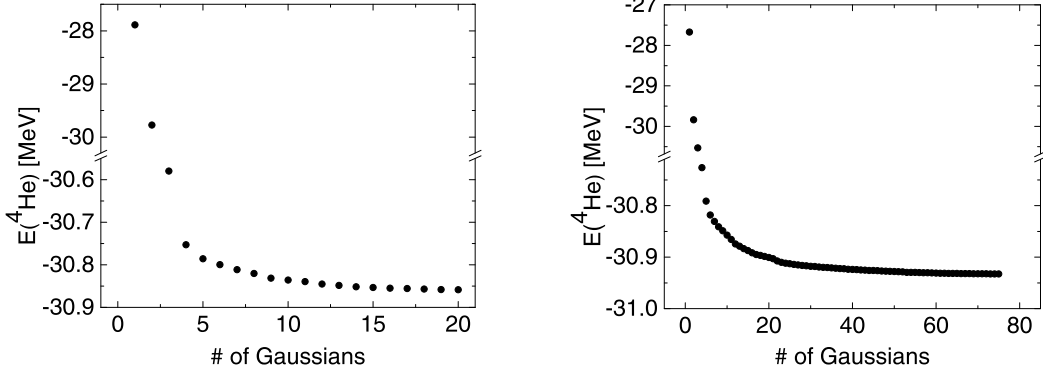


Figure 3. Convergence of the binding energy of  ${}^4\text{He}$ : MN (left) and MN-SO (right).

functionally very different valence part, and these two become completely entangled upon antisymmetrization. In addition, there does not seem to be an analytical way of computing matrix elements involving different core-valence permuted pieces of the wavefunction in Eq. (1). For these reasons, we are left with numerical evaluation of all matrix elements. For  ${}^6\text{He}$ , the integrals in Eq. (2) involve  $6 \times 3 = 18$  spatial and  $2 \times 6 = 12$  spin-isospin dimensions.

We use techniques of variational Monte Carlo (VMC) [ 9, 38, 39] to perform the variational search. The integration space is sampled statistically to find the regions most relevant for a given physical problem. In nuclear physics, VMC has been successfully applied to the problem of light nuclei [ 9]; however, the work here presented is novel in the choice of the trial wavefunction and therefore has its own challenges. In this section, we briefly mention the most important aspects of the optimization procedure, and advise the expert reader to [ 27] for a complete description.

The greatest challenge we faced was to develop a robust and yet efficient method to navigate the parameter space. This aspect falls beyond the framework of VMC. We found that optimization methods used in atomic and molecular physics [ 40, 41] did not work adequately for the problem at hand, most probably due to the specific nature of non-central, state-dependent nuclear interactions. In addition, due to the closeness to the three-body break-up threshold, an arbitrary starting wavefunction is inevitably three-body unbound. As a consequence, since the trial wavefunction drives the scanning of the integration space, all optimization methods tend to break the nucleus into the core and two individual neutrons as long as the system is three-body unbound. The easiest way to solve this pathological problem is to constrain the radius of the nucleus while performing the energy minimization above the three-body threshold. In our model, this is achieved most readily by taking the same non-linear parameters  $\rho_0$  in Eq. (15) for all valence terms. Once the system becomes three-body bound,  $\rho_0$ , still being the same in all valence terms, is adjusted to minimize the binding energy.

Different optimization procedures were used for the two interaction cases, MN and MN-SO, of  ${}^6\text{He}$ . In the absence of the spin-orbit force, the MN wavefunction contains

only spin-singlet valence terms. It is then possible to simply add hyper-angular and hyper-radial valence terms of increasing orders while re-adjusting  $\rho_0$  until convergence in the binding energy is reached, see Figure 4. Starting with a converged wavefunction, different values of  $\rho_0$  are tested using correlated sampling to finally locate the energy minimum, as shown in Figure 5. The converged MN wavefunction contains all spin-singlet valence terms with  $K \leq 12$  and  $n_{lag} \leq 5$  in both Y and T Jacobi bases. For the MN-SO case, the spin-singlet and spin-triplet valence states are mixed, and after antisymmetrization with the core, many components become almost orthogonal which creates numerical noise. It was for this reason that a more advanced optimization technique—comparative optimization on two independent random walks—needed to be developed. The energy minimum with  $\rho_0$  is first found for an auxiliary wavefunction as shown in Figure 5, and the MN-SO wavefunction is then tailored to the optimum value of  $\rho_0$ . Only valence terms lowering the energy the most are admitted to the MN-SO wavefunction at any optimization stage, or in other words  $n_{lag}$  and all components of  $\gamma_{val}$  in Eq. (15) are treated as discrete variational parameters. It takes ninety carefully selected valence terms with  $K \leq 14$  and  $n_{lag} \leq 5$  to reach energy convergence in the MN-SO case (see Figure 4). Due to a more selective optimization process, the MN-SO wavefunction contains fewer valence terms than its MN counterpart.

In both cases, the energy minimum in Figure 5 is located at  $\rho_0 \approx 0.45$  fm. In either case, the optimization begins with a valence term having low hyper-momentum  $K$  and  $n_{lag} = 0$ . Because of their diverging local kinetic energies near the origin, valence terms with  $n_{lag} \neq 0$  are avoided until preliminary convergence with  $K$  has been reached. To avoid high partial waves in the valence part, both Y and T Jacobi configurations are mixed. The linear coefficients  $c$  in Eq. (1) are determined via energy matrix diagonalization. To report final results, values of observables obtained on several independent random walks are averaged for precision. Due to the Monte Carlo integrations, all results come with statistical errors.

### 3.1. Three-body calculations

For comparison purposes, we repeat the inert-core three-body calculations for  ${}^6\text{He}$  published in [ 42]. Here, we make use of the valence basis introduced in Section 2.2. The phenomenological  ${}^4\text{He}$ -n interaction, vanishing for f- and higher-order partial waves, combines a spherically symmetric central Woods-Saxon and a spin-orbit Woods-Saxon-derivative parts with parameters taken from [ 42]. As for the interaction between valence neutrons, a realistic Gogny force is used [ 43]. Although the core-n and n-n two-body interactions reproduce  $\alpha$ -n and n-n phase shifts satisfactorily,  ${}^6\text{He}$  bound by these interactions would miss more than half of its experimental three-body binding energy of -0.97 MeV. As in [ 42], the problem of underbinding [ 2, 4] commonly encountered in three-body models based on inert cores is cured with an effective three-body force presumably simulating the effects of the closed  ${}^3\text{H}+{}^3\text{H}$  channel.

Three-body calculations were performed using the computer code EFADD [ 44]. The Pauli principle was satisfied by writing the wavefunction in the T Jacobi basis (see Section 2.2) and by projecting the forbidden core-n states before diagonalization [ 7]. Upon fitting the strength of the ambiguous three-body force, the converged three-body binding energy is -0.98 MeV for the wavefunction containing all valence terms with  $K \leq 40$

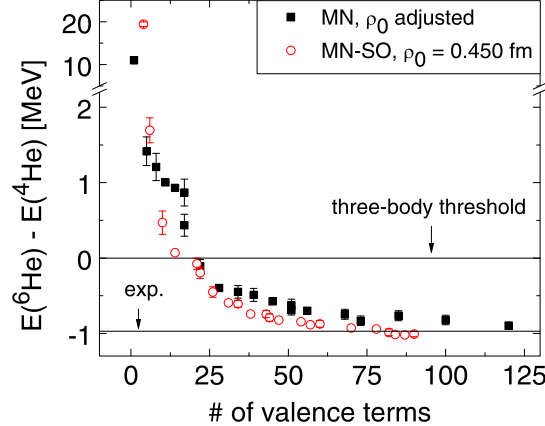


Figure 4. Convergence of the three-body binding energy with the number of valence terms included in Eq. (1). In case MN,  $\rho_0$  is adjusted along the optimization route; in case MN-SO, the results are for fixed  $\rho_0 = 0.45$  fm. Error bars were not computed for all points, and even when present they may be smaller than actual symbols.

and  $n_{lag} \leq 25$ . More three-body results are shown in Section 4 alongside with those from our microscopic model developed in this work.

In three-body models, the size of the core does not enter the actual calculations and some ad hoc assumption about the radius of the core is needed to estimate the size of the whole system. Then, the rms point proton  $\langle r_p^2 \rangle^{1/2}$  and rms point nucleon matter  $\langle r_m^2 \rangle^{1/2}$  radii of the three-body system (mass number  $A$ ) are related to those of the core (mass number  $A_{core}$ ) through:

$$\langle r_p^2 \rangle^{1/2} = \sqrt{\langle r_p^2(\text{core}) \rangle + \langle r_{\text{core-CMS}}^2 \rangle}, \quad \langle r_m^2 \rangle^{1/2} = \sqrt{\frac{1}{A} \left[ A_{core} \langle r_m^2(\text{core}) \rangle + \langle \rho^2 \rangle \right]}, \quad (26)$$

where  $r_{\text{core-CMS}}$  is the distance between the core's center of mass and the center of mass of the whole nucleus, and  $\langle \rangle$  denote expectation values.

## 4. Results

With the fully optimized wavefunctions, we calculate binding energies, rms radii, and density distributions, study core-valence antisymmetrization effects, and extract two-neutron overlap functions for  ${}^6\text{He}$ .

### 4.1. Energies and radii

Binding energies and radii for  ${}^4\text{He}$  and  ${}^6\text{He}$  from our calculations are shown in Table 1 along with experimental values and results obtained in the three-body model described in Section 3.1, SVM [ 19] representing microscopic cluster models, and ab-initio GFMC calculations [ 45]. In Table 1, experimental rms point proton radii  $\langle r_p^2 \rangle^{1/2}$  were computed

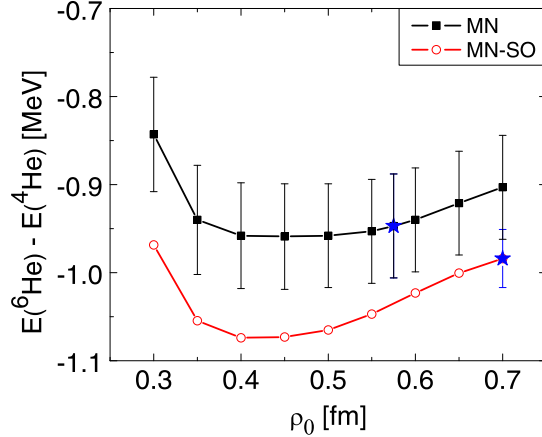


Figure 5. Dependence of the three-body binding energy of converged  ${}^6\text{He}$  on the non-linear parameter  $\rho_0$ . Both curves are constructed in correlated sampling on walks produced for reference values of  $\rho_0$  depicted by stars. In the MN-SO case, error bars could be computed for the reference  $\rho_0$  only.

from accurately measured charge radii  $\langle r_c^2 \rangle^{1/2}$  by using the relationship [ 46]:

$$\langle r_p^2 \rangle = \langle r_c^2 \rangle - \langle R_p^2 \rangle - \langle R_n^2 \rangle \frac{N}{Z}, \quad (27)$$

where  $\langle R_p^2 \rangle^{1/2} = 0.895(18)$  fm [ 47] is the rms charge radius of the proton,  $\langle R_n^2 \rangle = -0.120(5)$  fm $^2$  [ 48, 49] is the mean-square charge radius of the neutron, and  $N$  and  $Z$  are the neutron and proton numbers, respectively.

Based on arguments in Section 1 and Section 3.1, there is a qualitative difference between three-body and microscopic results in Table 1. Strictly speaking, the three-body results should be taken with caution because the three-body binding energy was fitted using an auxiliary three-body force of an arbitrary strength, while for radii we arbitrarily assumed the size of the core in Eq. (26) to be equal to that of our MN-SO  ${}^4\text{He}$ . The later assumption was made to ensure the best comparison between three-body and our results. Similar arbitrary assumptions are made for densities from the three-body model in Section 4.2.

In our model, a free  ${}^4\text{He}$  in Table 1 is overbound and smaller relative to experimental data which sets a wrong scale for absolute binding of  ${}^6\text{He}$ . We are, however, mostly interested in three-body-like features of  ${}^6\text{He}$  which should depend more on three-body rather than the absolute binding energy. As mentioned in Section 2.3, the mixture parameter in the Minnesota force was adjusted so that the three-body binding energy is about right. Upon this adjustment, there is no additional freedom in computing other observables.

Most likely due to the smaller  ${}^4\text{He}$  core, the MN and MN-SO proton radii of  ${}^6\text{He}$  are smaller than they should be. On the other hand, matter radii are comparable with those deduced from experiments. To assess how strongly the radii of  ${}^6\text{He}$  depend on the size of

Table 1

Absolute ( $E$ ) and three-body ( $E_{3body}$ ) binding energies in [MeV], and rms point nucleon (proton  $p$ , neutron  $n$ , matter  $m$ ) radii in [fm] of  $^4\text{He}$  and  $^6\text{He}$ . MN and MN-SO are results of this work; for other models, see text. Experimental proton radii were computed from Eq. (27) using charge radii from references cited in the table. Experimental rms neutron radii were computed from experimental values of proton and matter radii using  $\langle r_m^2 \rangle = (1/A)[Z\langle r_p^2 \rangle + N\langle r_n^2 \rangle]$ . The thickness of the neutron halo is defined as  $\Delta r = \langle r_n^2 \rangle^{1/2} - \langle r_p^2 \rangle^{1/2}$ .

		MN	MN-SO	3body	SVM	GFMC	exp.
$^4\text{He}$	$E$	-30.85	-30.93	N/A	-25.60	-28.37(3)	-28.30 [ 51]
	$\langle r_p^2 \rangle^{1/2}$	1.40	1.40	N/A	1.41	1.45(0)	1.46(1) [ 50]
	$E_{3body}$	-0.90(5)	-1.02(3)	-0.98	-0.96	-1.03(10)	-0.97 [ 52]
	$\langle r_m^2 \rangle^{1/2}$	2.41(1)	2.32(1)	2.49	2.42	2.55(1)	2.48(3) [ 53]
$^6\text{He}$	$\langle r_p^2 \rangle^{1/2}$	1.81(1)	1.75(1)	1.86	1.81	1.91(1)	1.91(2) [ 46]
	$\langle r_n^2 \rangle^{1/2}$	2.67(1)	2.56(1)	2.75	2.68	2.82(1)	2.72(4)
							2.51(6)
	$\Delta r$	0.86(1)	0.81(1)	0.89	0.87	0.91(1)	0.81(4)
							0.60(6)

the core, we turn to the three-body model. In a naive three-body picture based on Eq. (26), the larger size of  $^6\text{He}$  in the three-body model (when compared to MN and MN-SO) is solely due to the valence neutrons living on average slightly farther from the core. If the radius of the core is increased to its experimental value 1.46 fm, the three-body radii of  $^6\text{He}$  become  $\langle r_m^2 \rangle^{1/2} = 2.51$  fm,  $\langle r_p^2 \rangle^{1/2} = 1.90$  fm,  $\langle r_n^2 \rangle^{1/2} = 2.77$  fm, and  $\Delta r = 0.86$  fm, and the experimental proton radius of  $^6\text{He}$  would be seemingly reproduced. A similar shift towards larger radii could be expected for our results if larger cores were involved. Perhaps due to a stronger three-body binding, MN-SO  $^6\text{He}$  is slightly smaller than its MN counterpart, but the thickness of the neutron halo remains about the same.

Within SVM,  $^6\text{He}$  has been studied in the past repeatedly, e.g. [ 19, 55]. In Table 1, SVM results obtained in [ 19] for central and spin-orbit Minnesota and Coulomb interactions are quoted. In that reference, several different cluster compositions were considered to study break-up of the core in  $^6\text{He}$ . For  $^4\text{He}$ , we quote the results for the  $\alpha_2$  model where the  $^4\text{He}$  wavefunction is a superposition of three 0s-harmonic oscillator Slater determinants with common oscillator parameters. Due to this simple picture, SVM  $^4\text{He}$  is bound significantly less compared to MN and MN-SO cases. The SVM results for  $^6\text{He}$  in Table 1 are those from model (b) in [ 19]. In that model,  $^6\text{He}$  was described as a combination of  $^4\text{He} + n + n$  and  $^3\text{H} + ^3\text{H}$  with tritons again built from simple 0s-harmonic oscillators. The triton channel was introduced to overcome the insufficient three-body binding of  $^6\text{He}$ . SVM radii and three-body binding energies of  $^6\text{He}$  are comparable with ours, especially with the MN model.

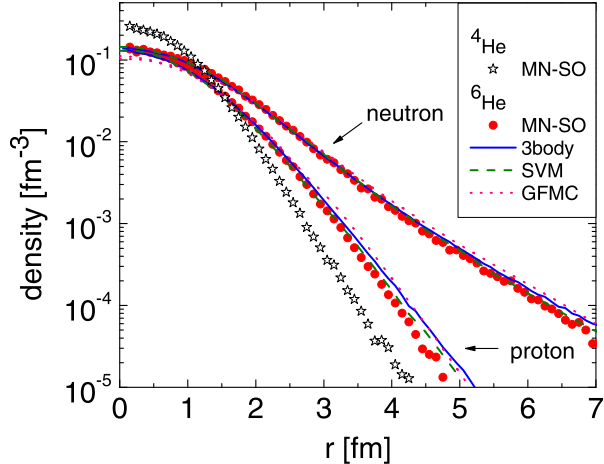


Figure 6. Point proton and neutron densities in  $^6\text{He}$  from models in Table 1 (except MN). SVM and GFMC densities are from [19] and [9], respectively; for densities from the three-body model, see text. For comparison, the proton (=neutron) density of the MN-SO  $^4\text{He}$  is shown. All proton (neutron) distributions are normalized to the number of protons (neutrons). Here,  $r$  is the distance from the center of mass.

For the sake of completeness, we also show ab-initio GFMC results in Table 1. These were obtained using realistic two-body AV18 and three-body IL2 interactions. The three-body binding energy for this case was computed by using  $E(^6\text{He}) = -29.4(1)$  MeV [45]. GFMC results are shown to point out that, by using modern realistic potentials in microscopic calculations, absolute binding energies and proton radii of  $^4\text{He}$  and  $^6\text{He}$  can indeed be reproduced. However, as we argued in Section 1 and unless proven otherwise, questions may arise about how well ab-initio models treat asymptotic regions so important for Borromean halo nuclei. Also, two-neutron overlap functions are yet to be extracted from ab-initio models of two-neutron halo nuclei.

#### 4.2. Density distributions

Point nucleon density distributions in  $^6\text{He}$  for the more realistic MN-SO case are plotted in Figure 6 along with those obtained from other models listed in Table 1. To compute densities from the three-body model, some assumption is needed about the internal structure of the core; quite arbitrarily, we computed these densities using an auxiliary microscopic wavefunction of the type of Eq. (1) constructed by combining the MN-SO  $^4\text{He}$  core and the three-body wavefunction serving as the valence part. Once again, this arbitrary construction reveals deficiencies in the few-body models.

The densities in Figure 6 from different models are close to one another with small differences reflecting different radii and wavefunction compositions. All models reproduce the most pronounced property, the neutron halo with the neutron distribution extending far beyond that of protons. Depleted at short distances, the proton density of  $^6\text{He}$  stretches farther out than that of  $^4\text{He}$ . A partial explanation of this effect comes from the three-

body model: in  ${}^6\text{He}$ , the  $\alpha$  core does not sit at the center of mass of the entire system, and its motion relative to the center of mass spreads out the proton distribution. Due to the same effect, the neutron density in  ${}^6\text{He}$  is also expected to be depleted at small distances relative to that of a free  ${}^4\text{He}$ , as is also visible in Figure 6.

### 4.3. Antisymmetrization effects

An important drawback of three-body models is the approximate way in which the Pauli principle between the core and the valence particles is taken into account [ 3]. The three-body procedure closest to the proper antisymmetrization is Feshbach projection where forbidden states are projected before diagonalization [ 7]. Given the similarities between the three-body basis and our valence basis, the effects of Pauli blocking can now be assessed microscopically from our model. This can be done simply by including or not including the core-valence antisymmetrizer  $\mathcal{A}^{\text{core-val}}$  in Eq. (1). Because of the simpler optimization procedure involved, we performed this study for the MN  ${}^6\text{He}$  only, but qualitatively the same outcome is also expected for the MN-SO case. See [ 27] for details.

The valence channels with  $K (= l_1 = l_2) = 0$  suffer the most from the core-valence Pauli blocking. When  $\mathcal{A}^{\text{core-val}}$  is not included and the  $K = 0$  valence channels are present in the wavefunction,  ${}^6\text{He}$  is three-body overbound by several tens of MeV. When all  $K = 0$  channels are removed, the nucleus becomes three-body unbound regardless of the inclusion of valence terms with higher hyper-momenta. When  $\mathcal{A}^{\text{core-val}}$  is active, converged  ${}^6\text{He}$  including  $K = 0$  valence channels is three-body bound by about -0.9 MeV as shown in Table 1. Upon removal of all  $K = 0$  channels from the converged wavefunction, the three-body binding reduces to about -0.75 MeV.

It is evident that the proper antisymmetrization is crucial for the structure of  ${}^6\text{He}$ . To produce a meaningful  ${}^6\text{He}$  it is not sufficient to simply neglect the most Pauli-blocked  $K = 0$  valence channels. Rather, all contributing valence channels ought to be included in the model space and carefully antisymmetrized. Given this conclusion, we strongly advocate using the best available Pauli blocking techniques in three-body models of halo nuclei.

### 4.4. Overlap functions

All models mentioned in Table 1, although different in their nature and predictive power, are in fair agreement on the most commonly computed properties of  ${}^6\text{He}$ . To appreciate the amount of microscopic details embedded in different models, it would be better to compare these models at the level of wavefunctions rather than highly integrated observables. In SVM, only s-wave overlap functions for  ${}^6\text{He}$  have been computed, but not expanded in hyper-spherical coordinates [ 55]; in GFMC, these functions are yet to be computed.

Here, we compare overlap functions (Section 2.4) computed for the MN-SO  ${}^6\text{He}$  to three-body wavefunctions (Section 3.1). In both cases, the  ${}^4\text{He}$  core is in its ground state. The three-body wavefunction is normalized to unity. For a meaningful interpretation of overlap functions, MN-SO wavefunctions of  ${}^4\text{He}$  and  ${}^6\text{He}$  in Eq. (20) need to be normalized to unity. For  ${}^4\text{He}$ , the normalization is known analytically from SVM; the norm of the  ${}^6\text{He}$  wavefunction was determined numerically with accuracy of 0.3% or better by using an auxiliary sampling function [ 27].

Table 2

Spectroscopic factors of the five dominant overlap channels in  ${}^6\text{He}$ . All channels are in the T Jacobi basis. Numbers in parentheses are relative errors.

channel						<i>S</i>		
	<i>K</i>	$l_1$	$l_2$	<i>L</i>	<i>S</i>	3body	MN-SO	MN-SO / 3body
$K = 2$ s-waves	2	0	0	0	0	0.8089	1.1155 (0.5%)	1.38
$K = 2$ p-waves	2	1	1	1	1	0.1103	0.1859 (0.7%)	1.69
$K = 0$ s-waves	0	0	0	0	0	0.0417	0.0555 (2.1%)	1.33
$K = 6$ d-waves	6	2	2	0	0	0.0164	0.0266 (3.5%)	1.62
$K = 6$ f-waves	6	3	3	1	1	0.0078	0.0122 (3.0%)	1.56
$\sum =$					0.9851	1.3957		

Ordered by spectroscopic factors, the five strongest overlap channels in the MN-SO  ${}^6\text{He}$  are listed in Table 2. These are the only channels that could be resolved, all other potential channels have spectroscopic factors too small and as such are buried in numerical noise. The table also contains three-body results; these were obtained by summing up all hyper-radial components in a given three-body channel. Not only the dominant channels are the same in the two models, but also the order of their spectroscopic strength is preserved. In the three-body model, these five channels account for more than 98% of the wavefunction. Therefore, we expect that these channels should also grasp most of the  ${}^4\text{He} + \text{n} + \text{n}$  decomposition of the MN-SO  ${}^6\text{He}$  ground state.

The hyper-radial dependence of overlap channels from Table 2 is shown in Figure 7 and Figure 8. We show these functions as  $u(\rho)$  because of their simpler asymptotic fall-off presented in Eq. (23). The three-body and our model agree on the overall shape of their hyper-radial distributions, and the number of nodes in those channels. On the other hand, our model appears to narrow the hyper-radial distributions and shift their peaks towards smaller distances, and to put more weight on smaller hyper-radii. This difference may be related to smaller radii of the MN-SO  ${}^6\text{He}$  in Table 1 when compared to those of the three-body model.

The most striking difference between our overlap functions and three-body wavefunctions is the normalization of their components quantified in Table 2 and visible in Figure 7 and Figure 8. The MN-SO spectroscopic factor for the strongest  $K = 2$  s-waves channel is greater than one due to recoil effects as the  ${}^4\text{He}$  core in Eq. (18) does not sit at the center of mass of  ${}^6\text{He}$ . These recoil effects are present in the three-body model too, but there the wavefunction as a whole is normalized to unity and so all spectroscopic factors are smaller than one. This deficiency of three-body models has been pointed out in [ 5] where an upper limit  $25/16=1.5625$  was derived for an additional renormalization factor to multiply the three-body spectroscopic factor as a mock-up for missing microscopic information. Indeed, our microscopic model consistently predicts spectroscopic factors greater by at least 30% than those obtained in the three-body model, but the increase varies between channels in a non-trivial manner as can be seen in Table 2. This observation suggests

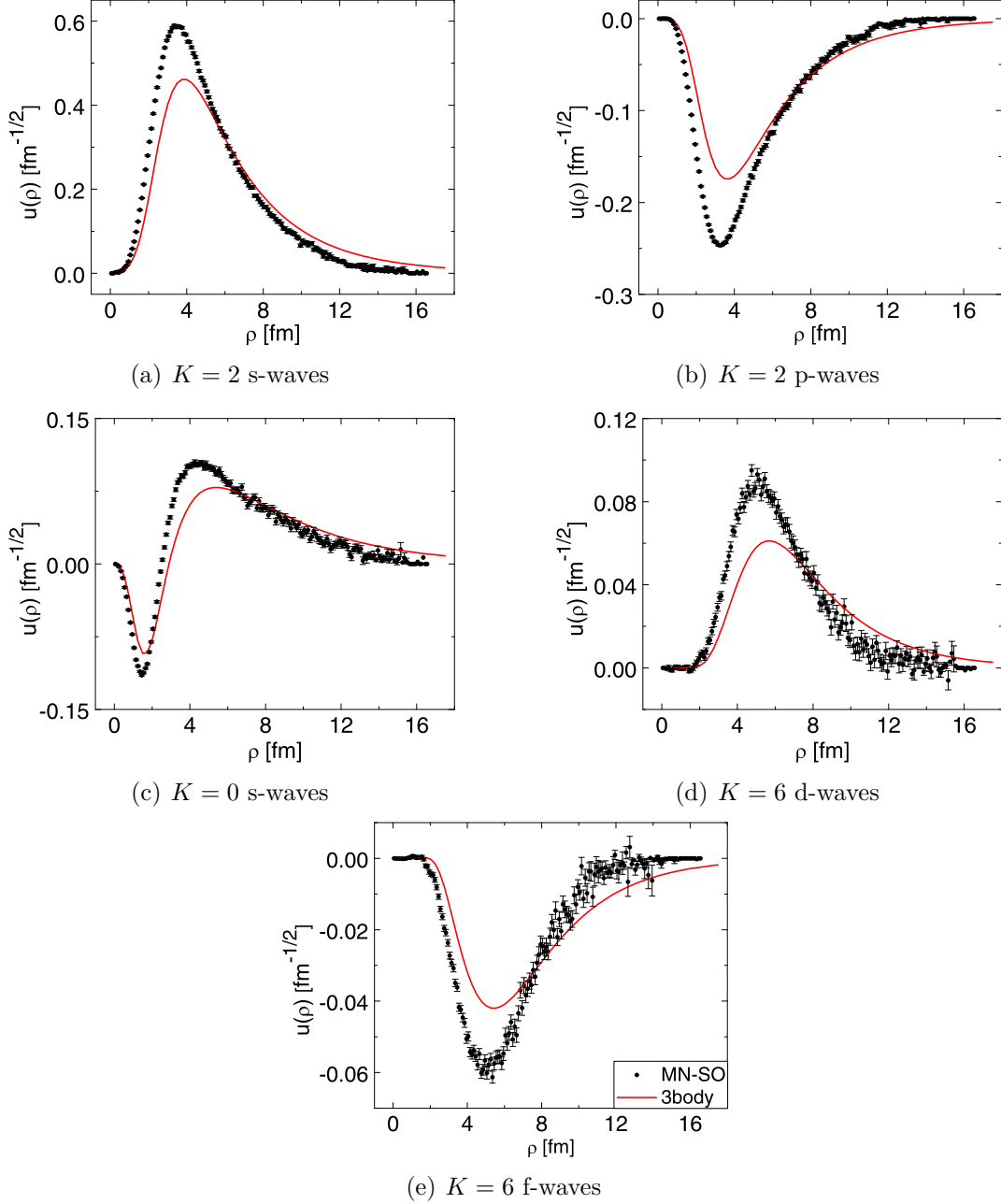


Figure 7. Hyper-radial dependence of overlap MN-SO functions and three-body wavefunctions for  ${}^6\text{He}$  for those channels presented in Table 2. The legend is the same in all panels.

that to account for microscopic effects, it may not be sufficient to simply renormalize the entire three-body wavefunction by a common factor (such as  $\sqrt{25/16}$  suggested in [ 5]). This conclusion is important, for example, for two-neutron transfer reaction theories for

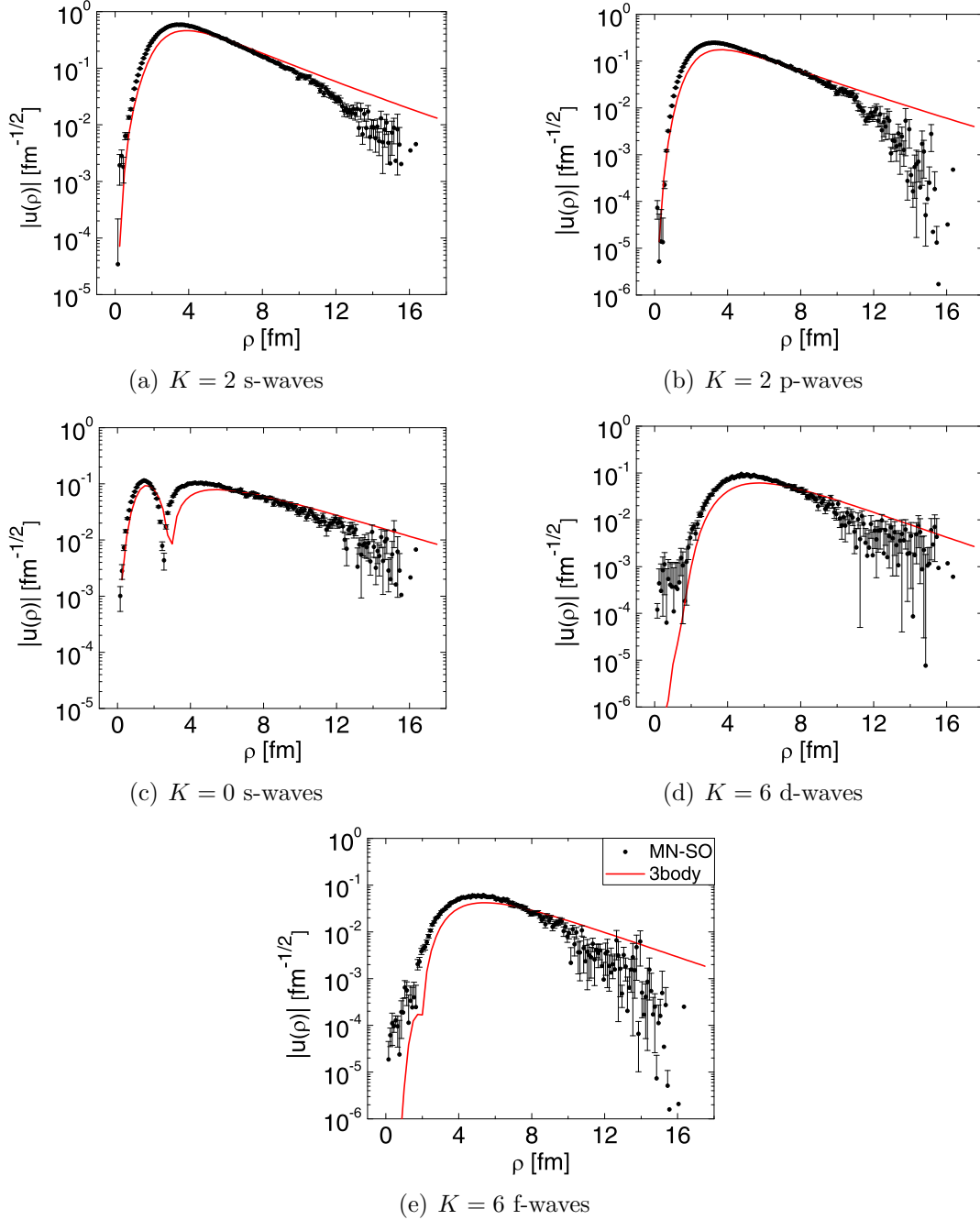


Figure 8. Hyper-radial dependence of absolute values of overlap MN-SO functions and three-body wavefunctions for  ${}^6\text{He}$  for those channels presented in Table 2. The legend is the same in all panels.

${}^6\text{He}$  in which three-body wavefunctions are traditionally used as structure input.

Since two-neutron transfer cross sections depend on spectroscopic factors, using micro-

scopically derived overlap functions instead of three-body wavefunctions would certainly have implications for reaction observables. For example, if the transfer reaction is mostly sensitive to the dominant component (s-waves) and peripheral, one might not see much change in the normalization, since the asymptotic parts of the overlaps do not significantly change. In the other hand, if the reaction is sensitive to the whole volume of the nucleus, one can expect a renormalization of the cross section consistent with the spectroscopic factors. Often, two-neutron transfer reactions are complicated by interference of various mechanisms. Preliminary two-nucleon transfer calculations for  ${}^6\text{He}(p,t){}^4\text{He}$  at  $E_{\text{lab}} = 25$  MeV involving the  ${}^6\text{He}$  microscopic overlap functions here presented have been performed assuming a 1-step reaction. However, any meaningful comparison with the data requires an extended study of the reaction mechanism which falls beyond the scope of this work.

At hyper-radii beyond about 12 fm, the MN-SO overlap functions in Figure 7 and Figure 8 become unreliable due to statistical fluctuations. Very large hyper-radii would place valence neutrons into regions very distant from the core, and because the Monte Carlo sampling probability is proportional to the wavefunction squared, such extreme spatial configurations are very unlikely to be visited by a walker during a random walk. Moreover, statistical samples in such distant regions may be highly correlated. For example, in extreme configurations of  ${}^6\text{He}$ , a hyper-radius of 12 fm corresponds to a di-neutron at a distance of 10.4 fm from the center of the core, or to two neutrons on opposite sides of the core, 17 fm apart.

In asymptotic regions, where the two valence neutrons are distant from the core, the core-valence antisymmetrization effects in Eq. (1) disappear. Then, both the three-body wavefunction and the overlap functions should fall off exponentially as shown in Eq. (9) and Eq. (23). For  $E_{3\text{body}} \approx -1$  MeV, we get  $\kappa \approx 0.22 \text{ fm}^{-1}$ . At larger hyper-radii in Figure 8, the three-body wavefunctions have the right slope still influenced by the three-body centrifugal barrier. Interestingly, we found in Section 3 the value  $\rho_0 = 0.45 \text{ fm}$  to be optimal for the valence part of the fully antisymmetrized wavefunction of  ${}^6\text{He}$ . By comparing Eq. (13) with Eq. (23), the two decay parameters can be related as  $\kappa = 1/(2\rho_0)$ . Then,  $\rho_0 = 0.45 \text{ fm}$  would correspond to  $\kappa = 1.11 \text{ fm}^{-1}$ , or  $E_{3\text{body}} \approx -25$  MeV. In other words, all individual valence terms in the MN-SO wavefunction decay much faster than the expected asymptotic form of overlap functions. Nevertheless, the strongest MN-SO overlap functions follow approximately the right long-range trend within the computationally safe region. Albeit the efforts in tailoring the basis to the problem, our results still show lingering differences in the asymptotics which could be improved by inclusion of Laguerre polynomials of even higher orders and/or by using a value of  $\rho_0 > 0.45 \text{ fm}$  in the MN-SO wavefunction.

Even though not discussed in detail, we also computed overlap functions for the MN case of  ${}^6\text{He}$ . Due to the absence of the spin-orbit force, valence spin-triplet states are missing in the MN wavefunction and consequently among overlap functions. Spectroscopic factors of spin-singlet channels were about the same as those for the MN-SO model in Table 2.

#### 4.5. Clusterization

Although  ${}^6\text{He}$  has been the object of many experimental studies (e.g. [ 56, 57]), there is still an ongoing debate on the neutron clusterization in this nucleus, namely on the

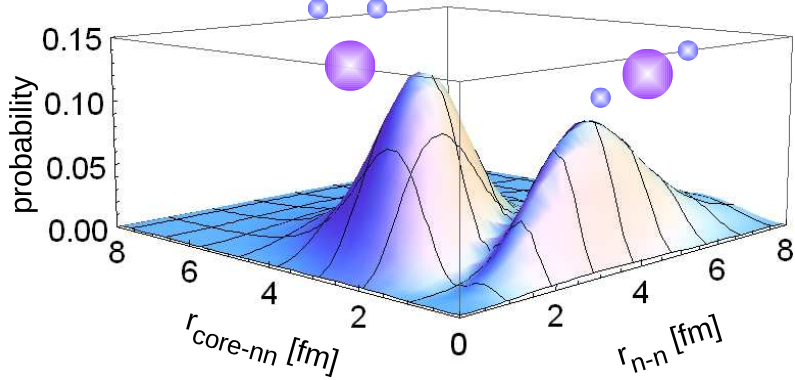


Figure 9. Correlation density plot for the ground state of  ${}^6\text{He}$  using MN-SO. Two dominant clustering patterns are shown schematically.

dominance of the cigar- or the di-neutron-like configuration. One way of gaining insight into this is by calculating the probability of finding the valence neutrons at definite places within the three-body-like decomposition defined in Eq. (21):

$$r_{n-n}^{r_2} r_{core-nn}^{r_2} \frac{1}{2J+1} \sum_{M_J} \left\langle \Psi_{J^\pi M_J T M_T}^{overlap} \left| \delta(r_{n-n} - r'_{n-n}) \delta(r_{core-nn} - r'_{core-nn}) \right| \Psi_{J^\pi M_J T M_T}^{overlap} \right\rangle, \quad (28)$$

where  $r_{n-n}$  and  $r_{core-nn}$  are the distance between valence neutrons and the distance between centers of masses of the core and the valence neutron pair, respectively. The integration in Eq. (28) is carried out over all (unprimed) degrees of freedom of all nucleons. The probability plot for the MN-SO  ${}^6\text{He}$  is presented in Figure 9. The figure indeed exhibits two peaks, as it should for a system dominated by  $K = 2$   $s$ -waves in the  $T$ -basis: a di-neutron-like peak positioned at about  $r_{n-n} = 1.93$  fm and  $r_{core-nn} = 2.63$  fm ( $\rho = 3.33$  fm) with the two neutrons close together and far from  ${}^4\text{He}$ , and a cigar-like peak at  $r_{n-n} = 3.82$  fm and  $r_{core-nn} = 1.03$  fm ( $\rho = 2.95$  fm) with the two neutrons positioned on opposite sides of the core. Qualitatively the same clustering picture has been predicted for example within three-body models [2] and SVM [55]. We looked into the clusterization probability distribution produced within the three-body model and found the peaks to be shifted to slightly larger radii (the di-neutron-like peak at  $r_{n-n} = 2.08$  fm and  $r_{core-nn} = 2.88$  fm and the cigar-like peak at  $r_{n-n} = 4.18$  fm and  $r_{core-nn} = 1.08$  fm) due to the three-body wavefunctions peaking at larger hyper-radii in Figure 7. Integrals under the peaks in the microscopic model are larger than those in the three-body model, consistent with the spectroscopic factors presented in Table 2: the integral under the di-neutron peak for the microscopic calculation is 0.85, compared to 0.60 in the three-body model and the integral under the cigar-like peak for the microscopic calculation is

0.54, compared to 0.38 in the three-body model. In both models, it appears that there is coexistence of the two clustering patterns, with 60% di-neutron and 40% cigar-like configurations.

## 5. Summary and Outlook

In this work, a microscopic structure model for light two-neutron halo nuclei is developed. Our goal was to combine advantages of few-body and microscopic methods to create a model capable to deal simultaneously with short- and characteristic long-range halo effects exhibited by these nuclei. To succeed, we combine the stochastic variational method and the hyper-spherical harmonic method into a fully antisymmetrized many-body approach. From the computational point of view, our model is similar to the variational Monte Carlo method, the novel feature being the form of the basis which incorporates the few-body features of two-neutron halo nuclei, in particular the correct behavior when the two halo neutrons are far from the core.

The model is applied to the ground state of  ${}^6\text{He}$  bound by an effective Minnesota nucleon-nucleon interaction including the spin-orbit force. When comparing three-body binding energies, radii, and densities, our results are comparable with those from other microscopic models using the same interaction. The overall binding energy is not reproduced as that would require more realistic forces, but this is not essential to produce the characteristic halo features determined by the binding relative to the three-body  ${}^4\text{He} + \text{n} + \text{n}$  threshold. The halo nature of the nucleus can be seen from its extended neutron density resulting in a large difference between the rms matter and proton radii. We advocate that the standard highly integrated observables, such as binding energies and radii, are not sensitive to details of the halo part of configuration space. To recognize these details, one should compare structure models at the level of wavefunctions or look at observables more sensitive to long-range correlations, such as reaction observables.

We properly calculate, to our knowledge for the first time, microscopic two-neutron overlap functions for  ${}^6\text{He}$  and compare them with those from the state-of-the-art three-body model. These overlap functions provide a crucial input to reaction calculations involving  ${}^6\text{He}$ , in particular to two-neutron transfer reaction models. As our basis was tailored specifically to capture the asymptotic behavior of the wavefunction, it is not surprising that the three-body wavefunction and the overlap functions are indeed similar in this region of coordinate space. In the range of the nuclear interaction, the three-body wavefunction seems to reproduce the properties of the many-body overlap functions only qualitatively. At a quantitative level, however, there are significant differences between overlap functions and three-body wavefunctions. Outstanding amongst these, the spectroscopic factor for the dominant microscopic overlap channel is larger by about 40% than its three-body counter-part. This discrepancy reveals the deficiency of three-body models, namely their inert-core approximation. Also, our study shows that the underbinding problem in three-body models comes partly from a poor treatment of antisymmetrization.

It is often thought that few-body models can be corrected for many-body effects by a simple renormalization of the wavefunction. However, we demonstrate that, in general, such a simple fix may not be sufficient because for the most important three-body-like components in  ${}^6\text{He}$ , the ratio between microscopic and three-body spectroscopic factors

varies between 1.3 and 1.7 in a nontrivial manner.

In this work we have shown that it is possible to obtain the correct long-range properties of halo nuclei within a fully microscopic approach. This opens up the opportunity to many applications. Studies of two-neutron transfer reactions involving  ${}^6\text{He}$  using our two-neutron overlap functions are underway. Given that in our model all matrix elements are calculated numerically, an extension of the method towards more realistic nuclear interactions should be straightforward. It would also be exciting to apply this method to heavier systems such as  ${}^{11}\text{Li}$  which would most likely entail more advanced optimization algorithms. On top of that, further code parallelization would be necessary to tackle the factorial growth in dimensionality of the problem.

### Acknowledgments

We thank Robert Wiringa and Steven Pieper for many discussions on VMC, Kalman Varga for discussions on SVM and for sharing his SVM code, and Ian Thompson for providing details on the previously published three-body results. The calculations were performed at the High Performance Computing Center at Michigan State University. This work was supported by the National Science Foundation through grant PHY-0555893 and the U.S. Department of Energy, Office of Nuclear Physics, under contracts DE-FG52-08NA28552 and DE-AC02-06CH11357.

## REFERENCES

1. A.S. Jensen et al., Rev. Mod. Phys. 76 (2004) 215.
2. M. Zhukov et al., Phys. Rep. 231 (1993) 151.
3. I.J. Thompson et al., Phys. Rev. C 61 (2000) 024318.
4. S. Funada, H. Kameyama, and Y. Sakuragi, Nucl. Phys. A 575 (1994) 93.
5. N.K. Timofeyuk, Phys. Rev. C 63 (2001) 054609.
6. N. Vinh Mau, Nucl. Phys. A 592 (1995) 33.
7. F.M. Nunes et al., Nucl. Phys. A 609 (1996) 43.
8. I. Brida, F.M. Nunes, and B.A. Brown, Nucl. Phys. A 775 (2006) 23.
9. S.C. Pieper and R.B. Wiringa, Ann. Rev. Nucl. Part. Sci. 51 (2001) 53.
10. S.C. Pieper, Nucl. Phys. A 751 (2005) 516.
11. P. Navrátil et al., J. Phys. G: Nucl. Part. Phys. 36 (2009) 083101.
12. P. Navrátil and B.R. Barrett, Phys. Rev. C 57 (1998) 3119.
13. P. Navrátil et al., Phys. Rev. Lett. 87 (2001) 172502.
14. H. Feldmeier and J. Schnack, Rev. Mod. Phys. 72 (2000) 655.
15. N. Itagaki, A. Kobayakawa, and S. Aoyama, Phys. Rev. C 68 (2003) 054302.
16. T. Neff, H. Feldmeier, and R. Roth, Nucl. Phys. A 752 (2005) 321.
17. K. Varga and Y. Suzuki, Phys. Rev. C 52 (1995) 2885.
18. Y. Suzuki and K. Varga, *Stochastic variational approach to quantum-mechanical few-body problems*, Springer-Verlag Berlin-Heidelberg, 1998.
19. K. Arai, Y. Suzuki, and R.G. Lovas, Phys. Rev. C 59 (1999) 1432.
20. K. Varga, Y. Suzuki, and R.G. Lovas, Phys. Rev. C 66 (2002) 041302.
21. S. Korennov and P. Descouvemont, Nucl. Phys. A 740 (2004) 249.
22. J.R. Armstrong, *A cluster model of  ${}^6\text{He}$  and  ${}^6\text{Li}$* , PhD thesis, Michigan State University, 2008.

sity, USA, 2007.

23. V. Vasilevsky et al., Phys. Rev. C 63 (2001) 034607.
24. K.M. Nollett, Phys. Rev. C 63 (2001) 054002
25. P. Navrátil, Phys. Rev. C 70 (2004) 054324
26. I. Brida and F.M. Nunes, Int. Jour. Mod. Phys. E 17 (2008) 2374.
27. I. Brida, *A microscopic hyper-spherical model of two-neutron halo nuclei*, PhD thesis, Michigan State University, USA, 2009.
28. A. Csótó, Phys. Rev. C 48 (1993) 165.
29. K. Varga, private communication, 2006.
30. I.J. Thompson, F.M. Nunes, and B.V. Danilin, Comp. Phys. Comm. 161 (2004) 87.
31. I.J. Thompson and F.M. Nunes, *Nuclear reactions for astrophysics*, Cambridge University Press, New York, 2009.
32. G. Erens, J.L. Visschers, and R. van Wageningen, Ann. Phys. 67 (1971) 461.
33. A.B. Volkov, Nucl. Phys. 74 (1965) 33.
34. D.R. Thompson, M. Lemere, and Y.C. Tang, Nucl. Phys. A 286 (1977) 53.
35. I. Reichstein and Y.C. Tang, Nucl. Phys. A 158 (1970) 529.
36. G.R. Satchler, *Direct nuclear reactions*, Oxford University Press, New York 1983.
37. J.M. Bang et al., Phys. Rep. 125 (1985) 253.
38. J.A. Carlson and R.B. Wiringa, Variational Monte Carlo techniques in nuclear physics, in *Computational nuclear physics I: Nuclear Structure*, edited by K. Langanke, J.A. Maruhn and S.E. Koonin, Springer-Verlag, 1991.
39. W.M.C. Foulkes et al., Rev. Mod. Phys. 73 (2001) 33.
40. X. Lin, H. Zhang and A.M. Rappe, J. Chem. Phys. 112 (2000) 2650.
41. C.J. Umrigar et al., Phys. Rev. Lett. 98 (2007) 110201.
42. D.V. Danilin et al., Nucl. Phys. A 632 (1998) 383.
43. D. Gogny, P. Pires and R.D. Tourtel, Phys. Lett. B 32 (1970) 591.
44. <http://www.fresco.org.uk/programs/efaddy/>
45. S.C. Pieper et al., Phys. Rev. C 64 (2001) 014001.
46. L.-B. Wang et al., Phys. Rev. Lett. 93 (2004) 142501.
47. I. Sick, Phys. Lett. B 576 (2003) 62.
48. S. Kopecky et al., Phys. Rev. Lett. 74 (1995) 2427.
49. S. Kopecky et al., Phys. Rev. C 56 (1997) 2229.
50. I. Sick, Phys. Rev. C 77 (2008) 041302.
51. D.R. Tilley, H.R. Weller and G.M. Hale, Nucl. Phys. A 541 (1992) 1.
52. D.R. Tilley et al., Nucl. Phys. A 708 (2002) 3.
53. I. Tanihata et al., Phys. Lett B 206 (1988) 592.
54. I. Tanihata et al., Phys. Lett B 289 (1992) 261.
55. K. Varga, Y. Suzuki, and Y. Ohbayasi, Phys. Rev. C 50 (1994) 189.
56. E. Sauvan et al., Phys. Rev. Lett. 87 (2001) 042501.
57. A. Chatterjee et al., Phys. Rev. Lett. 101 (2008) 032701.